Influence of the Yield Surface Curvature on the Forming Limit Diagrams Predicted by Crystal Plasticity Theory

Abstract

The aim of this paper is to investigate the impact of the microscopic yield surface (i.e., at the single crystal scale) on the forming limit diagrams (FLDs) of face centred cubic (FCC) materials. To predict these FLDs, the bifurcation approach is used within the framework of rate-independent crystal plasticity theory. For this purpose, two micromechanical models are developed and implemented. The first one uses the classical Schmid law, which results in the formation of vertices (or corners) at the yield surface, while the second is based on regularization of the Schmid law, which induces rounded corners at the yield surface. In both cases, the overall macroscopic behavior is derived from the behavior of the microscopic constituents (the single crystals) by using two different scale-transition schemes: the self-consistent approach and the Taylor model. The simulation results show that the use of the classical Schmid law allows predicting localized necking at realistic strain levels for the whole range of strain paths that span the FLD. However, the application of a regularized Schmid law results in much higher limit strains in the range of negative strain paths. Moreover, rounding the yield surface vertices through regularization of the Schmid law leads to unrealistically high limit strains in the range of positive strain paths.

Keywords

crystal plasticity, rate-independent theory, self-consistent model, Taylor model, bifurcation approach

H.K. Akpama
M. Ben Bettaieb
F. Abed-Meraim

LEM3, UMR CNRS 7239 - Arts et Métiers ParisTech, 4 rue Augustin Fresnel, 57078 Metz Cedex 3, France.
DAMAS, Laboratory of Excellence on Design of Alloy Metals for low-mAss Structures, Université de Lorraine, France
Holanyo.Akpama@ensam.eu
Mohamed.BenBettaieb@ensam.eu
Farid.Abed-Meraim@ensam.eu

http://dx.doi.org/10.1590/1679-78252456

Received 09.09.2015
In revised form 08.01.2016
Accepted 01.03.2016
Available online 09.03.2016

1 INTRODUCTION

During forming processes, metal sheet instabilities may occur in several ways. Though the origins of these instabilities are diverse and varied, they can be categorized into two main classes. The first class includes all instabilities that are basically related to the shape of the metal part and one refers to them as geometric instabilities. Buckling and wrinkling are typical examples of such geometric instabilities. The second class pertains to the instabilities that are intrinsically related to the material

behavior and one refers to them as material instabilities. The localization of deformation into narrow shear bands, as usually observed in three-dimensional solids, and localized necking in thin sheet metals are typical examples of material instabilities. In the literature, many investigations have been devoted to predicting the occurrence of localized necking, since this phenomenon is considered as limiting to material formability. In this field, we can quote the pioneering works of Keeler and Backofen (1963) and Goodwin (1968), who introduced the concept of forming limit diagram (FLD) to characterize the occurrence of localized necking in metal sheets. For each strain-path parameter ρ ranging from uniaxial tension ($\rho = -0.5$) to equibiaxial tension ($\rho = 1$), the in-plane principal strains, corresponding to the deformation state at the onset of localized necking, are reported on a curve designated as FLD. Accordingly, the deformation states below the FLD are expected to produce flawless parts, while the deformation states above the FLD may lead to potential defects. The FLDs can also be obtained experimentally; however, their experimental determination turns out to be complex and expensive. An interesting alternative to this experimental procedure is the numerical modeling approach. To set up this latter approach, two main ingredients are required: the modeling of the mechanical behavior of the studied sheet and a localization criterion, which is then coupled with the constitutive equations. In the related literature, several phenomenological and micromechanical models have been coupled to various localization criteria in order to predict FLDs for sheet metals. Among these diffuse or localized necking criteria, we can cite the maximum force principle initiated by Considère (1885), the imperfection approach developed by Marciniak and Kuczynski (1967), the bifurcation theory (Drucker, 1950; Drucker, 1956; Hill, 1958; Stören and Rice; 1975; Rice, 1976) and the perturbation method (Molinari and Clifton, 1987; Dudzinski and Molinari, 1991). A more detailed discussion along with a comparative analysis of the various plastic instability criteria can be found in Abed-Meraim et al. (2014). In the present work, attention will be restricted to the bifurcation approach developed by Stören and Rice (1975), which is adopted here as localization criterion. This approach is characterized by the formation of narrow localization bands corresponding to jumps in some constitutive rate-variables (e.g., strain rate tensor) across interfaces. Such material instability has also been shown to correspond to the loss of ellipticity of the partial differential equations governing the associated boundary value problem. The condition of strain localization is reached when the first zero eigenvalue is seen in the acoustic tensor (Rice, 1976).

From a numerical point of view, the bifurcation criterion is rather easy to implement compared to other localization criteria, such as the imperfection approach. However, without introducing some key destabilizing effects within the material constitutive modeling, the application of this theory unalterably predicts unrealistically high strain levels in the positive in-plane biaxial stretching range (see, e.g., Rice, 1976). In the case of phenomenological constitutive modeling, the destabilizing effects may be accounted for by introducing either damage-induced softening effects (Haddag et al., 2009; Mansouri et al., 2014) or by considering deviation from normality in the plastic flow rule (see, e.g., Rudnicki and Rice, 1975; Kuroda and Tvergaard, 2001). In the case of micromechanical modeling, the destabilizing mechanism is a natural outcome of crystal plasticity multislip and the associated yield surface vertex effects, which is accounted for by using the classical Schmid law (Schmid and Boas, 1935). The bifurcation approach has been successfully coupled in Franz et al. (2009a, 2009b) with a polycrystalline model based on the self-consistent scale-transition scheme within a fully three-dimensional framework. More recently, the bifurcation approach, under the plane-stress assumption,

has been applied in Yoshida and Kuroda (2012) to crystal plasticity based on classical Schmid's law and the full-constraint Taylor model. Furthermore, micromechanical models have the advantage of accounting for physical phenomena relevant at the single crystal scale, such as texture evolution, distribution of dislocation densities, morphological texture, residual stresses, in contrast to phenomenological models, for which some associated parameters do not have a direct physical meaning. However, the use of the classical Schmid law in micromechanical modeling is known to exhibit a major difficulty. Indeed, the application of classical Schmid's law leads in many cases to the well-known issue of ambiguity in the determination of the set of active slip systems and their corresponding slip rates. In the literature, this ambiguity problem has been tackled by a number of authors, and the most widely used remedy to eliminate the associated non-uniqueness in the selection of active slip systems is through the consideration of a rate-dependent approach. But, again, the use of a rate-dependent approach has also several shortcomings. On the one hand, the choice of rate-dependent modeling is not very realistic when the viscous effects are really limited. This is typically the case in cold forming processes. On the other hand, the use of elasto-viscoplastic behavior models in conjunction with the bifurcation approach leads to unrealistic limit strains for the whole range of strain paths (ranging from uniaxial tension to equibiaxial tension). To avoid at once the ambiguity in the determination of the set of active slip systems and the influence of undesirable viscous effects, the regularized Schmid law has been proposed as an interesting alternative to the classical Schmid law for the modeling of the mechanical behavior at the single crystal scale.

As discussed above, the application of the bifurcation approach leads to unrealistically high limit strains in the right-hand side of the FLD, when the flow theory with associative plasticity and smooth yield surface is used (Rice, 1976; Ben Bettaieb and Abed-Meraim, 2015). In the framework of micromechanical modeling, based on crystal plasticity, one can wonder how realistic the predicted FLDs would be if a rounded yield surface is used instead of the sharper yield surface associated with the classical Schmid law. One of the main objectives of the current work is to address this question. To this end, a regularized Schmid law, quite similar to that proposed by Gambin (1992), is adopted as plastic flow rule to model the single crystal response. The main feature of this regular form of the Schmid law is that its associated yield surface is practically the same as the classical Schmid yield surface, except that the corners are rounded. Both the Taylor model and the self-consistent scheme are used to derive the overall constitutive response of the polycrystal starting from the behavior of its microscopic components (single crystals). A similar behavior model has been proposed by Yoshida et al. (2009) to evaluate the response of an FCC rigid–plastic material under small strains.

The remainder of the paper is organized as follows:

- The second section will be devoted to the modeling of the single crystal behavior. Thereafter, a comparison will be performed between the classical Schmid law and the regularized Schmid law.
- In the third section, the theoretical framework for both homogenization models (namely, the Taylor model and the self-consistent approach) will be presented.
- In the fourth section, the bifurcation approach will be developed in the general framework, as well as its specialization to the plane-stress conditions.
- The fifth section details the numerical results at the macroscale and includes the corresponding comparisons and discussions.

Notations and conventions

CSL and RSL will be used hereafter as abbreviations for classical Schmid law and regularized Schmid law, respectively. As to the self-consistent model, it will be referred to as SC.

Vectorial and tensorial fields are designated by italic bold letters and symbols

Scalar variables and parameters are represented by italic thin letters and symbols

Einstein's convention of summation over repeated indices is adopted. The range of the free (resp. dummy) index is given before (resp. after) the corresponding equation

$\dot{\bullet}$	time derivative of $\bullet$
$\bullet^{-1}$	inverse of $\bullet$
$\bullet^{T}$	transpose of $\bullet$
$\bullet \,.\, \bullet$	inner product
$\bullet : \bullet$	double contraction product
$\bullet \otimes \bullet$	tensor product
$\det(\bullet)$	determinant of tensor $\bullet$
$\mathrm{sgn}(\bullet)$	sign of $\bullet$

2 MODELING OF THE SINGLE CRYSTAL BEHAVIOR

As a starting point, the total deformation gradient $\boldsymbol{f}$ is taken to be multiplicatively decomposed into an elastic part $\boldsymbol{f}^e$ and a plastic part $\boldsymbol{f}^p$

$$\boldsymbol{f} = \boldsymbol{f}^e.\boldsymbol{f}^p \tag{1}$$

The elastic part $\boldsymbol{f}^e$ may itself be multiplicatively decomposed into a stretching tensor $\boldsymbol{v}^e$ and a rotation tensor r

$$\boldsymbol{f}^e = \boldsymbol{v}^e.\boldsymbol{r} \tag{2}$$

Rotation r defines the orientation of the coordinate system related to the intermediate configuration relative to its counterpart in the current one.

The Eulerian velocity gradient $\boldsymbol{g}$, expressed in the current configuration, is therefore given by the following relation:

$$\begin{aligned} \boldsymbol{g} &= \dot{\boldsymbol{f}}.\boldsymbol{f}^{-1} = \dot{\boldsymbol{f}}^e.\boldsymbol{f}^{e^{-1}} + \boldsymbol{f}^e.\dot{\boldsymbol{f}}^p.\boldsymbol{f}^{p^{-1}}.\boldsymbol{f}^{e^{-1}} \\ &= \dot{\boldsymbol{v}}^e.\boldsymbol{v}^{e^{-1}} + \boldsymbol{v}^e.\dot{\boldsymbol{r}}.\boldsymbol{r}^T.\boldsymbol{v}^{e^{-1}} + \boldsymbol{v}^e.\boldsymbol{r}.\dot{\boldsymbol{f}}^p.\boldsymbol{f}^{p^{-1}}.\boldsymbol{r}^T.\boldsymbol{v}^{e^{-1}} \end{aligned} \tag{3}$$

As is the case for most metallic materials, the elastic deformation is often assumed to be very small compared to unity. Accordingly, the stretching tensor $\boldsymbol{v}^e$ is very close to the second-order identity tensor

$$\boldsymbol{v}^e \approx \mathbf{1} \tag{4}$$

Combining Eqs. (3) and (4), we obtain

$$\boldsymbol{g} = \dot{\boldsymbol{v}}^e + \dot{\boldsymbol{r}}.\boldsymbol{r}^T + \boldsymbol{r}.\dot{\boldsymbol{f}}^p.\boldsymbol{f}^{p^{-1}}.\boldsymbol{r}^T \tag{5}$$

The symmetric and skew-symmetric parts of $\boldsymbol{g}$, denoted as $\boldsymbol{d}$ and w, respectively, are defined by

$$\boldsymbol{d} = \frac{1}{2}(\boldsymbol{g} + \boldsymbol{g}^T) = \boldsymbol{d}^e + \boldsymbol{d}^p \quad ; \quad \boldsymbol{w} = \frac{1}{2}(\boldsymbol{g} - \boldsymbol{g}^T) = \boldsymbol{w}^e + \boldsymbol{w}^p \tag{6}$$

where the elastic and plastic parts, $\boldsymbol{d}^e$ and $\boldsymbol{d}^p$, of the strain rate tensor $\boldsymbol{d}$, as well as the elastic and plastic parts, $\boldsymbol{w}^e$ and $\boldsymbol{w}^p$, of the rotation rate tensor w are given by

$$\begin{aligned} &\boldsymbol{d}^e = \dot{\boldsymbol{v}}^e \quad ; \quad \boldsymbol{d}^p = \frac{1}{2}\boldsymbol{r}.(\dot{\boldsymbol{f}}^p.\boldsymbol{f}^{p^{-1}} + (\dot{\boldsymbol{f}}^p.\boldsymbol{f}^{p^{-1}})^T).\boldsymbol{r}^T \\ &\boldsymbol{w}^e = \dot{\boldsymbol{r}}.\boldsymbol{r}^T \quad ; \quad \boldsymbol{w}^p = \frac{1}{2}\boldsymbol{r}.(\dot{\boldsymbol{f}}^p.\boldsymbol{f}^{p^{-1}} - (\dot{\boldsymbol{f}}^p.\boldsymbol{f}^{p^{-1}})^T).\boldsymbol{r}^T \end{aligned} \tag{7}$$

In the current work, the plastic strain is assumed to be solely due to the slip on the crystallographic slip systems. Each slip system β is defined, in the deformed configuration, by two vectors $\vec{\boldsymbol{m}}^\beta$ and $\vec{\boldsymbol{n}}^\beta$ representing the slip direction and the normal to the slip plane, respectively. The symmetric and skew-symmetric parts of the tensor product $\vec{\boldsymbol{m}}^\beta \otimes \vec{\boldsymbol{n}}^\beta$ (which is known as the Schmid orientation tensor for slip system β), are denoted by $\boldsymbol{R}^\beta$ and $\boldsymbol{S}^\beta$, respectively. In the intermediate configuration related to the crystallographic lattice, the counterparts of $\vec{\boldsymbol{m}}^\beta$ and $\vec{\boldsymbol{n}}^\beta$ remain fixed throughout the deformation. They are denoted by $\vec{\boldsymbol{m}}_0^\beta$ and $\vec{\boldsymbol{n}}_0^\beta$, respectively. Similarly, the tensors corresponding to $\boldsymbol{R}^\beta$ and $\boldsymbol{S}^\beta$ in the intermediate configuration are denoted by $\boldsymbol{R}_0^\beta$ and $\boldsymbol{S}_0^\beta$, respectively. The relations between $\vec{\boldsymbol{m}}^\beta$ and $\vec{\boldsymbol{m}}_0^\beta$ as well as between $\vec{\boldsymbol{n}}^\beta$ and $\vec{\boldsymbol{n}}_0^\beta$ are given by the following expressions:

$$\vec{\boldsymbol{m}}^\beta = \boldsymbol{r}.\vec{\boldsymbol{m}}_0^\beta \quad ; \quad \vec{\boldsymbol{n}}^\beta = \vec{\boldsymbol{n}}_0^\beta.\boldsymbol{r}^{-1} \tag{8}$$

The detailed numbering of $\vec{\boldsymbol{m}}_0^\beta$ and $\vec{\boldsymbol{n}}_0^\beta$ for FCC single crystals is given in Appendix A.

As the plastic deformation is solely due to the slip on the crystallographic systems, tensors $\boldsymbol{d}^p$ and $\boldsymbol{w}^p$ can be expressed as

$$\begin{cases} \boldsymbol{d}^p = \dot{\gamma}^\beta \operatorname{sgn}(\tau^\beta)\boldsymbol{R}^\beta \\ \boldsymbol{w}^p = \dot{\gamma}^\beta \operatorname{sgn}(\tau^\beta)\boldsymbol{S}^\beta \end{cases} \quad ; \quad \beta = 1,...,N_s \tag{9}$$

where:

- $\dot{\gamma}^\beta$ is the absolute value of the slip rate on the slip system β. The algebraic values of the slip rates have the same sign as their respective resolved shear stresses, denoted τ^β.

- N_s is the total number of slip systems (equal to 12 for FCC single crystals).

In order to satisfy the objectivity principle, the lattice co-rotational derivative $\boldsymbol{\sigma}^{\nabla}$ of the Cauchy stress tensor $\boldsymbol{\sigma}$ is related to the elastic strain rate $\boldsymbol{d}^e$ by the following hypoelastic law:

$$\boldsymbol{\sigma}^{\nabla} = \dot{\boldsymbol{\sigma}} - \boldsymbol{w}^e.\boldsymbol{\sigma} + \boldsymbol{\sigma}.\boldsymbol{w}^e = \boldsymbol{\mathcal{C}}^e : \boldsymbol{d}^e \tag{10}$$

where $\boldsymbol{\mathcal{C}}^e$ is the fourth-order elasticity tensor.

The resolved shear stress τ^α is defined as the projection of the Cauchy stress tensor on the Schmid orientation tensor

$$\forall\, \alpha = 1,...,N_s : \quad \tau^\alpha = \boldsymbol{R}^\alpha : \boldsymbol{\sigma} \tag{11}$$

The rate form of Eq. (11) allows us to obtain $\dot{\tau}^\alpha$

$$\forall\, \alpha = 1,...,N_s : \quad \dot{\tau}^\alpha = \boldsymbol{R}^\alpha : \boldsymbol{\sigma}^{\nabla} \tag{12}$$

Combining Eqs. (12), (10), and $(9)_{(1)}$, $\dot{\tau}^\alpha$ can be expressed as

$$\begin{aligned} &\forall\, \alpha = 1,...,N_s : \\ &\dot{\tau}^\alpha = \boldsymbol{R}^\alpha : \boldsymbol{\mathcal{C}}^e : (\boldsymbol{d} - \operatorname{sgn}(\tau^\beta)\,\dot{\gamma}^\beta\, \boldsymbol{R}^\beta) = \tilde{\boldsymbol{R}}^\alpha : \boldsymbol{d} - \operatorname{sgn}(\tau^\beta)\,\dot{\gamma}^\beta \tilde{\boldsymbol{R}}^\alpha : \boldsymbol{R}^\beta \;\; ; \;\; \beta = 1,...,N_s \end{aligned} \tag{13}$$

where $\tilde{\boldsymbol{R}}^\alpha$ is equal to $\boldsymbol{R}^\alpha : \boldsymbol{\mathcal{C}}^e$.

The evolution of the critical shear stress is given by the following hardening law:

$$\forall\, \alpha = 1,...,N_s : \quad \dot{\tau}_c^\alpha = H^{\alpha\beta}\,\dot{\gamma}^\beta \quad ; \quad \beta = 1,...,N_s \tag{14}$$

where $\boldsymbol{H}$ is a hardening matrix, whose analytical expression will be given in details in Appendix A.

The constitutive law of the single crystal relates the nominal stress rate $\dot{\boldsymbol{n}}$ to the velocity gradient $\boldsymbol{g}$, using the microscopic tangent modulus $\boldsymbol{l}$

$$\dot{\boldsymbol{n}} = \boldsymbol{l} : \boldsymbol{g} \tag{15}$$

To derive the analytical expression of $\boldsymbol{l}$, one has to express the slip rates in terms of the velocity gradient

$$\forall\, \alpha = 1,...,N_s : \quad \dot{\gamma}^\alpha = \boldsymbol{\mathcal{Y}}^\alpha : \boldsymbol{d} = \boldsymbol{\mathcal{Y}}^\alpha : \boldsymbol{g} \tag{16}$$

where $\boldsymbol{\mathcal{Y}}^\alpha$ is a second-order symmetric tensor, corresponding to slip system α, whose expression will be given later, as it depends on the plastic flow rule considered (i.e., classical Schmid law or regularized one).

The analytical expression for the microscopic tangent modulus reads

$$\boldsymbol{l} = \boldsymbol{\mathcal{C}}^e + \boldsymbol{\sigma} \otimes \boldsymbol{1} - {}^1_{\boldsymbol{\sigma}}\boldsymbol{L} - {}^2_{\boldsymbol{\sigma}}\boldsymbol{L} - \operatorname{sgn}(\tau^\alpha)(\boldsymbol{\mathcal{C}}^e : \boldsymbol{R}^\alpha + \boldsymbol{S}^\alpha.\boldsymbol{\sigma} - \boldsymbol{\sigma}.\boldsymbol{S}^\alpha) \otimes \boldsymbol{\mathcal{Y}}^\alpha \;; \quad \alpha = 1,...,N_s \tag{17}$$

where ${}^{1}_{\boldsymbol{\sigma}}\boldsymbol{L}$ and ${}^{2}_{\boldsymbol{\sigma}}\boldsymbol{L}$ are fourth-order tensors that contain convective terms of Cauchy stress components

$$ {}^{1}_{\boldsymbol{\sigma}}L_{ijkl} = \frac{1}{2}(\delta_{lj}\sigma_{ik} - \delta_{kj}\sigma_{il}) \quad ; \quad {}^{2}_{\boldsymbol{\sigma}}L_{ijkl} = \frac{1}{2}(\delta_{ik}\sigma_{lj} + \delta_{il}\sigma_{kj}) \tag{18} $$

Depending on the plastic flow rule considered, which may involve CSL or RSL, different analytical expressions for $\boldsymbol{\mathcal{Y}}^{\alpha}$ can be obtained. These expressions will be derived in Sections 2.1 and 2.2.

2.1 Plastic Flow Rule Associated with the Classical Schmid Law

In this section, the slip rates are derived from the classical Schmid law (Schmid and Boas, 1935). This law states that slip may occur on a given slip system α only if the absolute value of its resolved shear stress τ^{α} reaches its critical value τ_c^{α}

$$ \forall\, \alpha = 1,...,N_s : \quad \begin{cases} \left|\tau^{\alpha}\right| < \tau_c^{\alpha} \;\Rightarrow\; \dot{\gamma}^{\alpha} = 0 \\ \left|\tau^{\alpha}\right| = \tau_c^{\alpha} \;\Rightarrow\; \dot{\gamma}^{\alpha} \geq 0 \end{cases} \tag{19} $$

Accordingly, the CSL corresponds to a multi-surface yield criterion, where each slip system α is defined by a yield function χ^{α}

$$ \forall\, \alpha = 1,...,N_s : \quad \chi^{\alpha} = \left|\tau^{\alpha}\right| - \tau_c^{\alpha} \leq 0 \tag{20} $$

A global yield function can therefore be defined as

$$ f = (\mathrm{Max}_{\alpha=1,...,N_s}\, \chi^{\alpha}) \leq 0 \tag{21} $$

It is noteworthy that the CSL satisfies the normality rule. Indeed, one can easily verify that Eq. $(9)_{(1)}$ is equivalent to

$$ \boldsymbol{d}^{p} = \dot{\gamma}^{\beta}\, \frac{\partial \chi^{\beta}}{\partial \boldsymbol{\sigma}} \quad ; \quad \beta = 1,...,N_s \tag{22} $$

In order to compute the slip rates, the consistency condition is used

$$ \forall\, \alpha \in \mathcal{A} : \quad \dot{\chi}^{\alpha} = \dot{\tau}^{\alpha}\, \mathrm{sgn}(\tau^{\alpha}) - \dot{\tau}_c^{\alpha} = 0 \tag{23} $$

where $\mathcal{A}$ is the set of active slip systems ($\alpha \in \mathcal{A} \Leftrightarrow \dot{\gamma}^{\alpha} > 0$).

One obtains eventually

$$ \begin{aligned} \forall\, \alpha \in \mathcal{A} : \quad \dot{\gamma}^{\alpha} &= M^{\alpha\beta}\, \mathrm{sgn}(\tau^{\beta})\, \boldsymbol{R}^{\beta} : \boldsymbol{\mathcal{C}}^{e} : \boldsymbol{d} \quad ; \quad \beta \in \mathcal{A} \\ &= \boldsymbol{\mathcal{Y}}^{\alpha} : \boldsymbol{d} \end{aligned} \tag{24} $$

where $\boldsymbol{M}$ is the inverse of matrix $\boldsymbol{P}$ defined by the following index form:

$$\forall\, \alpha,\beta \in \mathcal{A}: \quad P^{\alpha\beta} = (H^{\alpha\beta} + \mathrm{sgn}(\tau^{\alpha})\,\mathrm{sgn}(\tau^{\beta})\,\boldsymbol{R}^{\alpha} : \boldsymbol{\mathcal{C}}^{e} : \boldsymbol{R}^{\beta}) \tag{25}$$

$\boldsymbol{\mathcal{Y}}^{\alpha}$ being the second-order symmetric tensor used in Eqs. (16) and (17).

When the CSL is used, the analytical expression of $\boldsymbol{\mathcal{Y}}^{\alpha}$ is given as follows:

$$\begin{aligned} &\forall\, \alpha \in \mathcal{A}: \quad \boldsymbol{\mathcal{Y}}^{\alpha} = M^{\alpha\beta}\,\mathrm{sgn}(\tau^{\beta})\,\boldsymbol{R}^{\beta} : \boldsymbol{\mathcal{C}}^{e} \quad ; \quad \beta \in \mathcal{A} \\ &\forall\, \alpha \notin \mathcal{A}: \quad \boldsymbol{\mathcal{Y}}^{\alpha} = \boldsymbol{0} \end{aligned} \tag{26}$$

2.2 Plastic Flow Rule Associated with the Regularized Schmid Law

The regular form of the Schmid law (RSL) is drawn from the work of Gambin (1992). The corresponding yield function reads

$$f = \sum_{\alpha=1}^{N_s} \left(\frac{\tau^{\alpha}}{\tau_c^{\alpha}} \right)^{2n} - 1 \leq 0 \tag{27}$$

where n is a positive number acting as a regularization parameter. As will be shown in Section 2.3, this parameter accounts for the sharpness of the yield surface.

Contrarily to the CSL, for which the computation of the slip rates requires matrix inversion, the slip rates have the following generic form in the present case:

$$\forall\, \alpha = 1,...,N_s: \quad \dot{\gamma}^{\alpha} = \dot{\lambda}\, \frac{\mathrm{sgn}(\tau^{\alpha})}{\tau_c^{\alpha}} \left(\frac{\tau^{\alpha}}{\tau_c^{\alpha}} \right)^{2n-1} \tag{28}$$

where $\dot{\lambda}$ is a positive scalar, which is derived from the normality rule. Indeed, the normality rule states that there exists a positive value $\dot{\omega}$ such that

$$\begin{aligned} \boldsymbol{d}^{p} &= \dot{\omega} \frac{\partial f}{\partial \boldsymbol{\sigma}} = \dot{\omega} \frac{\partial f}{\partial \tau^{\alpha}} \frac{\partial \tau^{\alpha}}{\partial \boldsymbol{\sigma}} \\ &= \dot{\omega} \frac{2n}{\tau_c^{\alpha}} \left(\frac{\tau^{\alpha}}{\tau_c^{\alpha}} \right)^{2n-1} \boldsymbol{R}^{\alpha} = 2n\dot{\omega} \frac{\mathrm{sgn}(\tau^{\alpha})}{\tau_c^{\alpha}} \left(\frac{\tau^{\alpha}}{\tau_c^{\alpha}} \right)^{2n-1} \mathrm{sgn}(\tau^{\alpha})\,\boldsymbol{R}^{\alpha} \quad ; \quad \alpha = 1,...,N_s \end{aligned} \tag{29}$$

By taking $\dot{\lambda} = 2n\dot{\omega}$, one obtains relation $(9)_{(1)}$. In order to derive the analytical expression of the plastic multiplier $\dot{\lambda}$, the consistency condition is used

$$\dot{f} = 2n \sum_{\alpha=1}^{N_s} \left(\frac{\dot{\tau}^{\alpha}}{\tau^{\alpha}} - \frac{\dot{\tau}_c^{\alpha}}{\tau_c^{\alpha}} \right) \left(\frac{\tau^{\alpha}}{\tau_c^{\alpha}} \right)^{2n} = 0 \tag{30}$$

Furthermore, by using Eqs. (13), (14), and (28), one obtains the following relation:

$$\forall\, \alpha = 1,...,N_s: \quad \frac{\dot{\tau}^{\alpha}}{\tau^{\alpha}} - \frac{\dot{\tau}_c^{\alpha}}{\tau_c^{\alpha}} = \frac{\tilde{\boldsymbol{R}}^{\alpha} : \boldsymbol{d}}{\tau^{\alpha}} - \dot{\lambda} \sum_{\delta=1}^{N_s} \frac{\mathrm{sgn}(\tau^{\delta})}{\tau_c^{\delta}} \left(\frac{\tau^{\delta}}{\tau_c^{\delta}} \right)^{2n-1} \left(\frac{\tilde{\boldsymbol{R}}^{\alpha} : \boldsymbol{R}^{\delta}}{\tau^{\alpha}} + \frac{H^{\alpha\delta}}{\tau_c^{\alpha}} \right) \tag{31}$$

Combining Eqs. (30) and (31), the analytical expression of $\dot{\lambda}$ is eventually obtained

$$\dot{\lambda} = \frac{\boldsymbol{\mathcal{F}} : \boldsymbol{d}}{k_0} \tag{32}$$

where $\boldsymbol{\mathcal{F}}$ is a second-order symmetric tensor defined as

$$\forall\, i,j = 1,2,3: \quad \mathcal{F}_{ij} = \sum_{\alpha=1}^{N_s} \left(\frac{\tau^\alpha}{\tau_c^\alpha} \right)^{2n} \frac{\tilde{R}_{ij}^\alpha}{\tau^\alpha} \tag{33}$$

and k_0 is a scalar defined as

$$k_0 = \sum_{\alpha=1}^{N_s} \sum_{\delta=1}^{N_s} \frac{\mathrm{sgn}(\tau^\delta)}{\tau_c^\delta} \left(\frac{\tau^\alpha}{\tau_c^\alpha} \right)^{2n} \left(\frac{\tau^\delta}{\tau_c^\delta} \right)^{2n-1} \left(\frac{\tilde{\boldsymbol{R}}^\alpha : \boldsymbol{R}^\delta}{\tau^\alpha} + \frac{H^{\alpha\delta}}{\tau_c^\alpha} \right) \tag{34}$$

Once the plastic multiplier $\dot{\lambda}$ is calculated (through Eqs. (32)-(34)), the slip rate on each slip system can be determined using Eq. (28)

$$\begin{aligned} \forall\, \alpha = 1,\ldots,N_s: \quad \dot{\gamma}^\alpha &= \left[\frac{\mathrm{sgn}(\tau^\alpha)}{k_0 \tau_c^\alpha} \left(\frac{\tau^\alpha}{\tau_c^\alpha} \right)^{2n-1} \right] \boldsymbol{\mathcal{F}} : \boldsymbol{d} \\ &= \boldsymbol{\mathcal{Y}}^\alpha : \boldsymbol{d} \end{aligned} \tag{35}$$

Recall that tensor $\boldsymbol{\mathcal{Y}}^\alpha$ is used in Eq. (17) for the determination of the microscopic tangent modulus. In the framework of RSL, the analytical expression of $\boldsymbol{\mathcal{Y}}^\alpha$ reads

$$\forall\, \alpha = 1,\ldots,N_s: \quad \boldsymbol{\mathcal{Y}}^\alpha = \left[\frac{\mathrm{sgn}(\tau^\alpha)}{k_0 \tau_c^\alpha} \left(\frac{\tau^\alpha}{\tau_c^\alpha} \right)^{2n-1} \right] \boldsymbol{\mathcal{F}} \tag{36}$$

The generic form of Eq. (28) is quite similar to that used for visco-plastic materials. We briefly recall the analytical expression of the slip rates in the framework of rate-dependent theory (Asaro and Needleman, 1985)

$$\forall\, \alpha = 1,\ldots,N_s: \quad \dot{\gamma}^\alpha = \dot{\gamma}^0 \left(\frac{\tau^\alpha}{\tau_c^\alpha} \right)^{1/m} \tag{37}$$

where $\dot{\gamma}^0$ is a reference shear rate and m the rate-sensitivity parameter.

Although similar in form, a major difference between the rate-dependent formulation (see Eq. (37)) and the RSL (see Eq. (28)) is that the latter preserves its rate-independent character and, hence, it is still applicable to bifurcation analysis, while the former is not. It must also be noted that, from a numerical point of view, forms (28) and (37) generally lead to very stiff equations, especially when exponents $2n$–1 and $1/m$ take high values. Consequently, the CPU time required to integrate the constitutive equations based on the regularized form of the Schmid law is generally high. This CPU time is quite comparable to that required for the integration of visco-plastic single crystal models,

when the value of exponent $2n$–1 (in the regularized form (28)) becomes very close to the magnitude of exponent $1/m$ in the visco-plastic evolution law (37).

2.3 Comparison Between the CSL and the RSL

As pointed out by several authors (Gambin and Barlat, 1997; Imbault and Arminjon, 1998), the value of the regularization parameter n determines the degree of sharpness of the yield surface. The higher the value, the sharper the corresponding yield surface. From a certain value of n, the obtained yield surfaces are very close to that determined by CSL. This feature is illustrated in Figure 1, where the RSL-based yield surfaces for an FCC single crystal, corresponding to two different values of n (namely, n=5 and n=20), are compared with the CSL-based yield surface. The three Euler angles that define the initial crystallographic orientation of the single crystal (Bunge, 1968) are randomly chosen and are respectively equal to 293°, 124°, and 305°. The Young modulus is equal to 210 GPa and the Poisson ratio is equal to 0.3. The hardening parameters τ_0, h_0, n_1 (see Appendix A for more details) are equal to 40 MPa, 390 MPa, and 0.35, respectively.

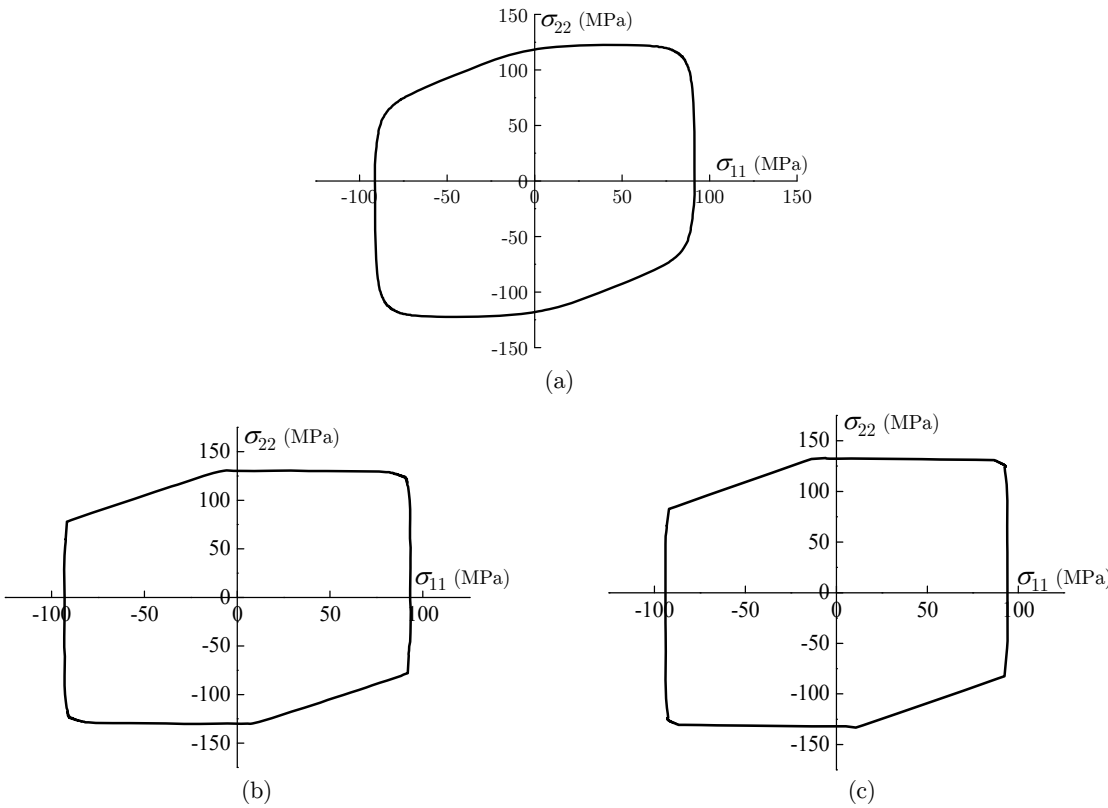

Figure 1: Comparison between the RSL yield surfaces, corresponding to two different values for the regularization parameter, and the CSL yield surface: (a) RSL (n=5); (b) RSL (n=20); (c) CSL.

Figure 2(a) depicts the stress–strain uniaxial tensile response as obtained with both flow rules (CSL and RSL). For n=5, the RSL-based response is significantly different from its counterpart

yielded by CSL. Nevertheless, for $n = 500$, the RSL-based curve matches the CSL-based one for a certain range of strain (0 up to 0.2). Beyond 0.2, the deviation between the two tensile responses is a consequence of slip system activity, which is not the same in both models. Figure 2(b) shows the evolution of some components of the microscopic tangent modulus as a function of the tensile strain. We can observe that for the RSL, the evolution of the tangent modulus components is independent of the regularization parameter n. Compared to CSL, we can see that there is only a difference in the shearing components, where those predicted by CSL are reduced beyond the elastic range, whereas those determined by RSL keep their elastic values. These qualitative comparisons are consistent with those reported by Yoshida et al. (2009) in the framework of small strains.

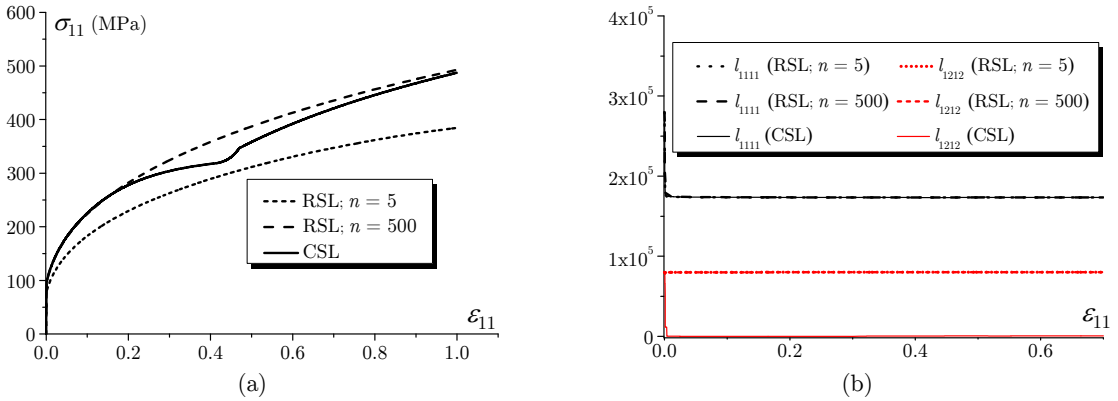

Figure 2: Uniaxial tensile test for an FCC single crystal: (a) Stress–strain responses; (b) Components of the single crystal tangent modulus.

3 MODELING OF THE POLYCRYSTAL BEHAVIOR

In this section, we briefly present the incremental self-consistent scheme used to derive the macroscopic tangent modulus $\boldsymbol{\mathcal{L}}$. The latter relates the macroscopic nominal stress rate tensor $\dot{\boldsymbol{N}}$ to the macroscopic velocity gradient $\boldsymbol{G}$

$$\dot{\boldsymbol{N}} = \boldsymbol{\mathcal{L}} : \boldsymbol{G} \tag{38}$$

This scheme has been initially developed by Hill (1965a, 1965b), in the framework of small elastoplastic strain, and extended by Lipinski (Lipinski and Berveiller, 1989; Lipinski et al., 1995) to large deformation. Using this scale-transition scheme, the macroscopic tangent modulus is obtained by the following relation:

$$\boldsymbol{\mathcal{L}} = f^I \; \boldsymbol{l}^I : \boldsymbol{A}^I \quad ; \quad I = 1,...,N_g \tag{39}$$

where f^I represents the volume fraction of grain I, $\boldsymbol{l}^I$ its microscopic tangent modulus, while $\boldsymbol{A}^I$ denotes the concentration tensor that relates the microscopic velocity gradient $\boldsymbol{g}^I$ to its macroscopic

counterpart $\boldsymbol{G}$. When the Taylor model is considered, Eq. (39) is still valid provided that the concentration tensor $\boldsymbol{A}^I$ of each grain I be replaced by the fourth-order identity tensor $\boldsymbol{I}$.

4 THEORETICAL FRAMEWORK FOR THE PLANE-STRESS BIFURCATION APPROACH

Figure 3 illustrates the localization of deformation in a metal sheet, which is represented by a localization band defined by its unit normal vector $\vec{\mathcal{N}}$.

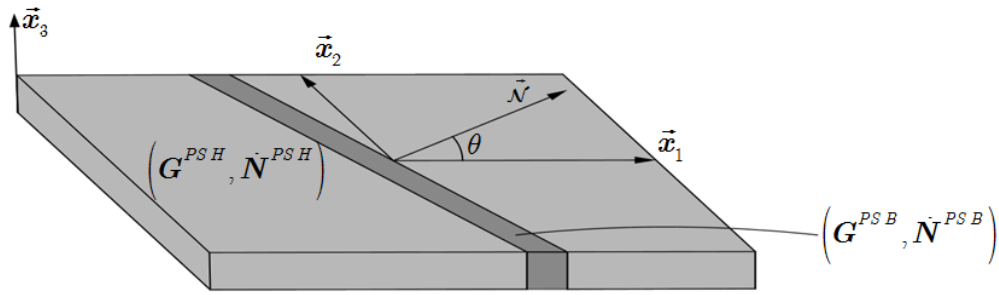

Figure 3: Illustration of localized necking in a metal sheet.

In the current study, the three-dimensional formulation of the bifurcation approach implemented in Franz et al. (2009a, 2013) is adapted to the plane-stress framework. With the plane-stress condition, the nominal stress rate tensor and the velocity gradient satisfy the following mixed boundary conditions:

$$\boldsymbol{G} = \begin{pmatrix} 1 & 0 & 0 \\ 0 & \rho & 0 \\ 0 & 0 & ? \end{pmatrix} \quad ; \quad \dot{\boldsymbol{N}} = \begin{pmatrix} ? & ? & 0 \\ ? & ? & 0 \\ 0 & 0 & 0 \end{pmatrix} \tag{40}$$

where ρ is the strain-path parameter, and symbol $?$ designates the unknown components. Though in the present work the adopted tangent modulus is different from that developed in Franz et al. (2009a, 2013), the bifurcation criterion has the same form

$$\det\left(\vec{\mathcal{N}} \,.\boldsymbol{\mathcal{L}}^{PS}.\vec{\mathcal{N}}\right) = 0 \tag{41}$$

where $\boldsymbol{\mathcal{L}}^{PS}$ is the 2D tangent modulus that relates the in-plane components of the nominal stress rate tensor to the in-plane components of the velocity gradient. The analytical expression for the 2D tangent modulus $\boldsymbol{\mathcal{L}}^{PS}$ is derived from the general expression of the 3D tangent modulus $\boldsymbol{\mathcal{L}}$ by the classical relation

$$\forall \alpha,\beta,\gamma,\delta = 1,2: \quad \mathcal{L}^{PS}_{\alpha\beta\gamma\delta} = \mathcal{L}_{\alpha\beta\gamma\delta} - \frac{\mathcal{L}_{\alpha\beta 33}\,\mathcal{L}_{33\gamma\delta}}{\mathcal{L}_{3333}} \tag{42}$$

5 NUMERICAL RESULTS AT THE MACROSCALE

In this section, we investigate the influence of both flow rules (namely, the CSL and the RSL models) on the overall stress–strain responses as well as on the predicted FLDs at the polycrystal scale. As a starting point, an FCC polycrystalline aggregate composed of 1000 grains is considered. The hardening parameters as well as the elastic constants are the same as those used in Section 2.3. Figure 4 shows the random initial texture taken for this polycrystal.

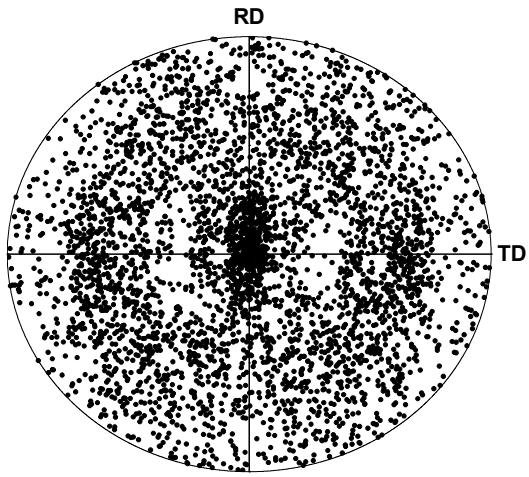

Figure 4: {111} Pole figure for the initial texture (1000 grains).

Figure 5 compares the stress–strain responses, obtained with both flow rules, for three different in-plane strain paths ρ: uniaxial tensile test ($\rho = -0.5$), plane-strain tension ($\rho = 0$), and positive biaxial stretching ($\rho = 0.5$). For the RSL, the regularization parameter n that measures the sharpness of the corresponding yield surface is set to 20. This value is motivated by a reasonable compromise between the computation time and the stress–strain curve matching of both flow rules. Indeed, the computation time increases significantly with the value of n, because the time step requires to be divided into several sub-increments in order to accurately satisfy the yield criterion. For all the computations related to the RSL presented hereafter, parameter n is fixed to 20. In Figure 5(a), the Taylor model is used as homogenization scheme. From this figure, one can observe that at large strains, the gap between the RSL and the CSL-based responses increases as the strain-path parameter ρ increases. However, in the small strain range, it is found that both flow rules yield the same response, as previously mentioned by Yoshida et al. (2009). In Figure 5(b), the SC model is used to assess the macroscopic behavior of the material. In this latter case, except for the uniaxial tensile test, the deviations between the RSL and CSL occur at much earlier stage of deformation, with a softer response yielded by the CSL. On the other hand, comparisons between the Taylor model and the SC scheme (see, e.g., Figures 5(a) and 5(b)) reveal that the use of the RSL leads to the same overall stress–strain response, irrespective of the homogenization model, whereas the use of CSL leads to a softer response with the SC approach. These observations are fully consistent with those made by Yoshida et al. (2009).

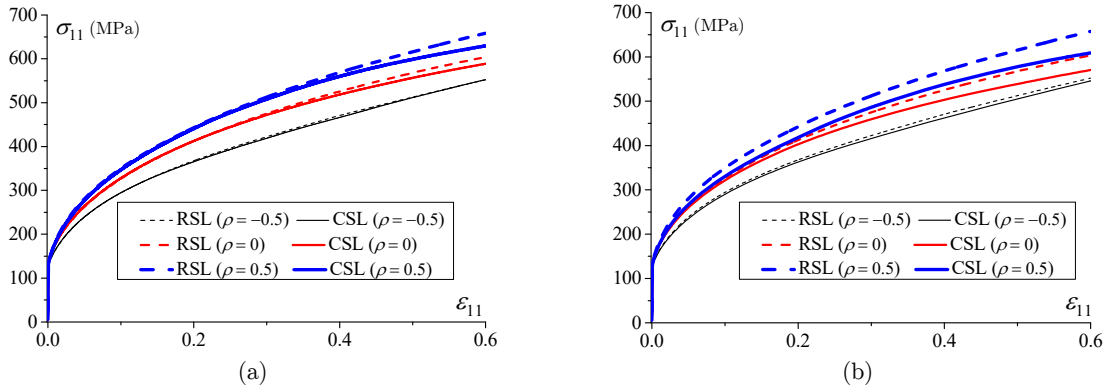

Figure 5: Overall stress–strain responses for three different in-plane loading paths: (a) Taylor model; (b) Self-consistent model.

Figure 6 depicts the evolution of some components of the tangent modulus as function of the major strain. It is well-known that the incremental elasto-plastic tangent modulus plays a major role in the framework of bifurcation theory. In this regard, the evolution of the components $\mathcal{L}_{1111}$, $\mathcal{L}_{1122}$, and $\mathcal{L}_{1212}$, which are representative of the other components, is investigated. It is worth noting that, in the case of RSL, the predicted components keep their high elastic values in the course of loading. Quite the opposite trend is observed with the CSL, where the shearing components of the tangent modulus, represented by $\mathcal{L}_{1212}$, are significantly reduced beyond the elastic range of deformation. In spite of this significant reduction in the shear components, notice that the stress–strain responses yielded by both flow rules are practically the same with the Taylor model (see, e.g., Figure (5)).

Figures 7 and 8 show the evolution of the minimum of the determinant of the acoustic tensor, over all possible band orientations, as a function of the major strain, for different strain paths. In Figure 7, the Taylor model is used as scale-transition scheme. Recall that strain localization is marked by the singularity of the acoustic tensor (i.e., as soon as its determinant reaches zero). In the range of negative strain paths (see, e.g., $\rho = -0.5$ and $\rho = 0$), we observe a quasi-continuous drop in the determinant of the acoustic tensor, for both flow rules, which regularly decreases and eventually reaches zero. However, for positive strain paths ($\rho > 0$), the trend is completely different for the RSL framework, in which the determinant decreases very slightly for $\rho = 0.1$ and keeps practically a constant value for $\rho = 1$ or $\rho = 0.5$. As discussed in the literature, most often within phenomenological constitutive frameworks (see, e.g., Rice, 1976; Hutchinson and Neale, 1978; Ben Bettaieb and Abed-Meraim, 2015), it is found that when the shearing components of the tangent modulus keep their high elastic values, the use of bifurcation theory as localization criterion yields unrealistically high localization strains in the positive biaxial stretching range. Here, the localization predictions suggest values for the critical strains far beyond 2. In Figure 8, the same analysis as that conducted in Figure 7 is followed, but with the SC model as homogenization scheme. As can be observed, the SC approach (see Figure 8) reveals trends quite similar to those reflected by the Taylor model. Besides, for the CSL, the predicted localization strains given by the SC model are much lower in the

whole than those obtained with the Taylor model. For the RSL, however, there are no significant differences between the Taylor and the SC localization predictions.

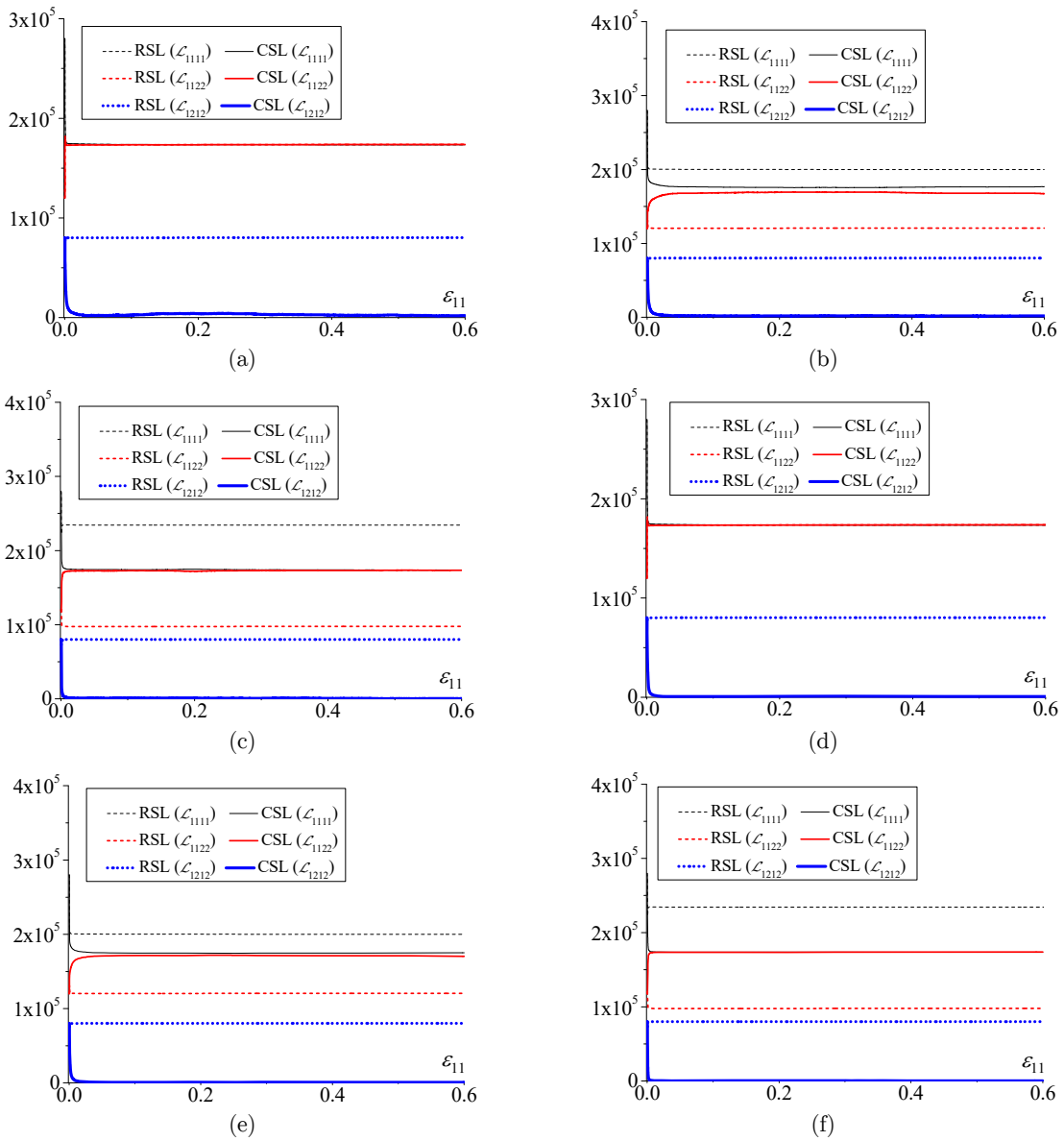

Figure 6: Evolution of the components of the tangent modulus for different strain paths: (a) Taylor model ($\rho = -0.5$); (b) SC model ($\rho = -0.5$); (c) Taylor model ($\rho = 0$); (d) SC model ($\rho = 0$); (e) Taylor model ($\rho = 0.5$); (f) SC model ($\rho = 0.5$).

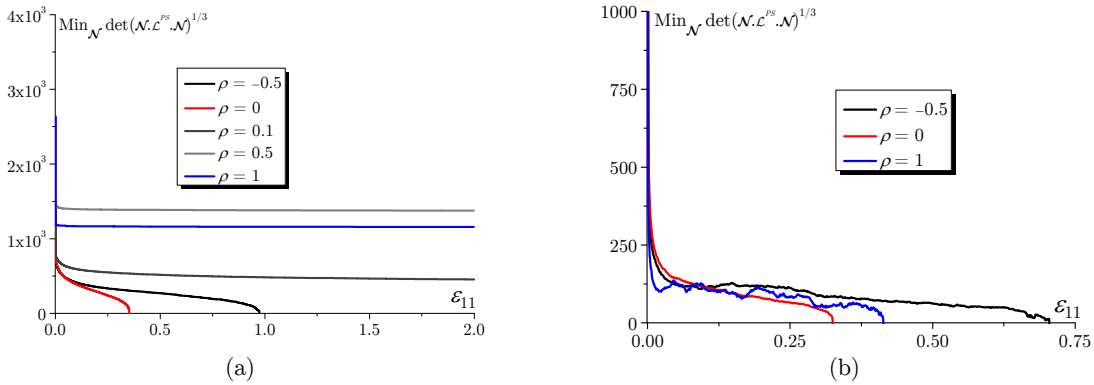

Figure 7: Evolution of the minimal determinant of the acoustic tensor for different strain paths: (a) RSL (n=20) coupled with the Taylor model; (b) CSL coupled with the Taylor model.

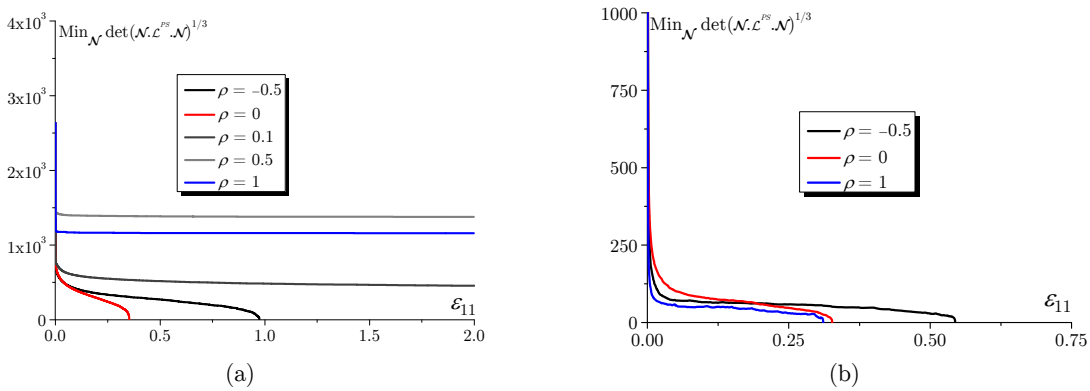

Figure 8: Evolution of the minimal determinant of the acoustic tensor for different strain paths: (a) RSL (n=20) coupled with the SC model; (b) CSL coupled with the SC model.

Figure 9 displays the localized necking strains predicted for all of the strain paths ranging from uniaxial tension ($\rho = -0.5$) to equibiaxial expansion ($\rho = 1$). The two homogenization models (namely, the Taylor and SC scale-transition schemes) are coupled with both plastic flow rules (i.e., CSL and RSL). As previously mentioned, the limit strains predicted by the RSL are extremely high in the range of positive in-plane biaxial stretching. This trend is consistent with the observations made in Figure 6, where it was shown that the shearing components of the tangent modulus keep their elastic values when the RSL is used, which leads to unrealistically high limit strains in the positive biaxial stretching range. In the negative strain-path range, however, the RSL necking strains are predicted at realistic levels, although they are much higher than those obtained with the CSL (see Figure 9).

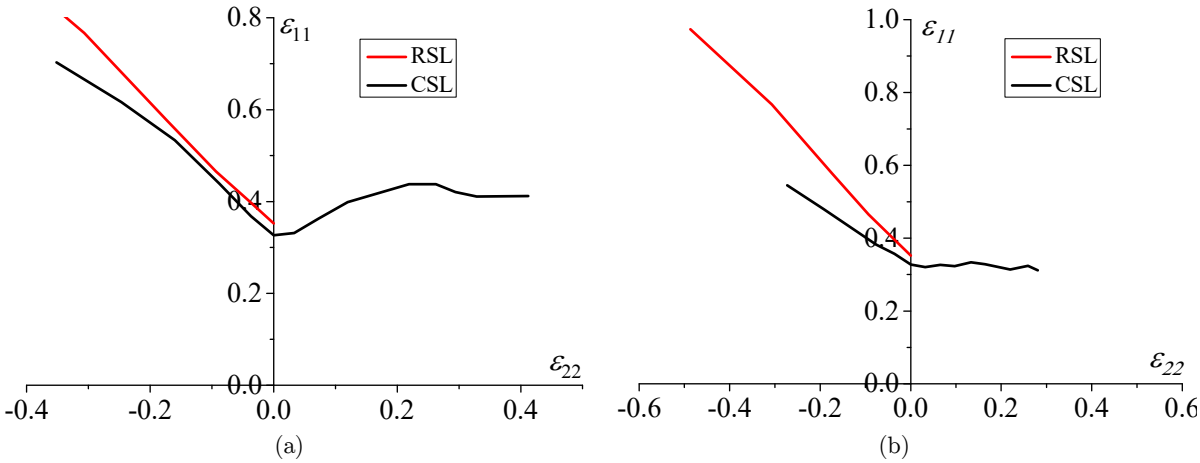

Figure 9: FLDs predicted by the two different homogenization models for both plastic flow rules: (a) Taylor model; (b) SC model.

Figure 10 shows the evolution of the localization band orientation, corresponding to the predicted FLDs, as function of the strain-path parameter ρ. With the Taylor model, the predicted band orientations are almost the same for both plastic flow rules in the range of negative strain paths ($\rho < 0$) (see Figure 10(a)). For the SC model, however, the differences in terms of predicted band orientations are more noticeable in the range of negative strain paths (see Figure 10(b)). Also, with the SC approach, and for the studied polycrystalline aggregate (see its initial texture shown in Figure 4), the localization bands predicted by the CSL are found to remain always normal to the major strain direction in the range of positive strain paths ($\rho > 0$).

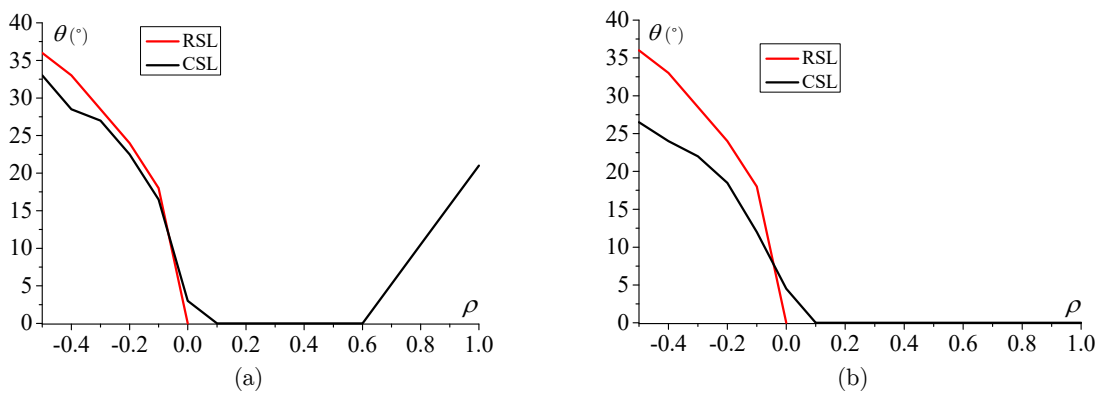

Figure 10: Critical band orientations as predicted by: (a) Taylor model; (b) SC model.

6 CONCLUDING REMARKS

The effect of the plastic flow rule, as modeled at the single crystal scale, on the forming limit diagrams of polycrystalline sheet metals has been investigated using the bifurcation approach as localization criterion. To this end, two different plastic flow rules have been considered at the single crystal scale.

The first one is based on the classical Schmid law, which results in a yield surface with sharp vertices, while the other uses a regular form of the Schmid law, which leads to a smoother yield surface (i.e., with rounded vertices). In both cases, the Taylor model as well as the self-consistent scale-transition scheme are used to relate the micro and macro scales. From the numerical results, it is found that, in the range of negative strain paths, the FLDs predicted by the regularized Schmid law are realistic, although much higher than those predicted by the classical Schmid law, and this conclusion is valid irrespective of the scale-transition scheme considered (Taylor model or incremental self-consistent approach). However, in the range of positive strain paths, the predicted limit strains given by the regularized Schmid law are unrealistically high, in contrast to those obtained by the classical Schmid law, which remain quite realistic. It is also found that when the regularized Schmid law is used, the overall stress–strain response of the material as well as the predicted necking strains are almost insensitive to the scale-transition scheme, at variance with the use of the classical Schmid law.

References

Abed-Meraim, F., Balan, T., Altmeyer, G. (2014). Investigation and comparative analysis of plastic instability criteria: application to forming limit diagrams. International Journal of Advanced Manufacturing Technology 71:1247–1262.

Asaro, R.J., Needleman, A. (1985). Texture development and strain hardening in rate dependent polycrystals. Acta Metallurgica 33:923–953.

Ben Bettaieb, M., Abed-Meraim, F. (2015). Investigation of localized necking in substrate-supported metal layers: Comparison of bifurcation and imperfection analyses. International Journal of Plasticity 65:168–190.

Bunge, H.J. (1968). The orientation distribution function of the crystallites in cold rolled and annealed low-carbon steel sheets. Physica Status Solidi (b) 26:167–172.

Considère, A. (1885). Mémoire sur l'emploi du fer et de l'acier dans les constructions. Annales des Ponts et Chaussées 9:574–775.

Drucker, D.C. (1950). Some implications of work hardening and ideal plasticity. Quarterly of Applied Mathematics 7:411–418.

Drucker, D.C. (1956). On the uniqueness in the theory of plasticity. Quarterly of Applied Mathematics 16:35–42.

Dudzinski, D., Molinari, A. (1991). Perturbation analysis of thermoviscoplastic instabilities in biaxial loading. International Journal of Solids and Structures 27:601–628.

Franz, G., Abed-Meraim, F., Ben Zineb, T., Lemoine, X., Berveiller, M. (2009b). Strain localization analysis using a multiscale model. Computational Materials Science 45:768–773.

Franz, G., Abed-Meraim, F., Berveiller, M. (2013). Strain localization analysis for single crystals and polycrystals: Towards microstructure-ductility linkage. International Journal of Plasticity 48:1–33.

Franz, G., Abed-Meraim, F., Lorrain, J.P., Ben Zineb, T., Lemoine, X., Berveiller, M. (2009a). Ellipticity loss analysis for tangent moduli deduced from a large strain elastic–plastic self-consistent model. International Journal of Plasticity 25:205–238.

Gambin, W. (1992). Refined analysis of elastic–plastic crystals. International Journal of Solids and Structures 29:2013–2021.

Gambin, W., Barlat, F. (1997). Modeling of deformation texture development based on rate independent crystal plasticity. International Journal of Plasticity 13:75–85.

Goodwin, G.M. (1968). Application of strain analysis to sheet metal forming problems in press shop. Metallurgia Italiana 60:767–744.

Haddag, B., Abed-Meraim, F., Balan, T. (2009). Strain localization analysis using a large deformation anisotropic elastic–plastic model coupled with damage. International Journal of Plasticity 25:1970–1996.

Hill, R. (1958). A general theory of uniqueness and stability in elastic–plastic solids. Journal of the Mechanics and Physics of Solids 6:239–249.

Hill, R. (1965a). Continuum micro-mechanics of elastoplastic polycrystals. Journal of the Mechanics and Physics of Solids 13:89–101.

Hill, R. (1965b). A self consistent mechanics of composite materials. Journal of the Mechanics and Physics of Solids 13:213–221.

Hutchinson, J.W., Neale, K.W. (1978). Sheet Necking – II. Time-independent behavior. In: D.P. Koistinen, N.M. Wang (Eds.), Mechanics of sheet metal forming. New York: Plenum Press, 127–153.

Imbault, D., Arminjon, M. (1998). Deformation textures of fcc materials predicted with a regular form of the Schmid law. Materials Science Forum 273:371–376.

Keeler, S.P., Backofen, W.A. (1963). Plastic instability and fracture in sheets stretched over rigid punches. Trans. ASM 56:25–48.

Lipinski, P., Berveiller, M. (1989). Elastoplasticity of micro-inhomogeneous metals at large strains. International Journal of Plasticity 5:149–172.

Lipinski, P., Berveiller, M., Reubrez, E., Morreale, J. (1995). Transition theories of elastic–plastic deformation of metallic polycrystals. Archive of Applied Mechanics 65:291–311.

Mansouri, L.Z., Chalal, H., Abed-Meraim, F. (2014). Ductility limit prediction using a GTN damage model coupled with localization bifurcation analysis. Mechanics of Materials 76:64–92.

Marciniak, Z., Kuczynski, K. (1967). Limit strains in processes of stretch-forming sheet metal. International Journal of Mechanical Sciences 9:609–620.

Molinari, A., Clifton, R. (1987). Analytical characterization of shear localization in thermo-visco-plastic solids. Journal of Applied Mechanics 54:806–812.

Rice, J.R. (1976). The localization of plastic deformation. In: 14th International Congress of Theoretical and Applied Mechanics 207–220.

Schmid, E., Boas, W. (1935). Plasticity of Crystals. Chapman and Hall, London.

Stören, S., Rice, J.R. (1975). Localized necking in thin sheets. Journal of the Mechanics and Physics of Solids 23:421–441.

Yoshida, K., Brenner, R., Bacroix, B., Bouvier, S. (2009). Effect of Regularization of the Schmid Law on self-consistent estimates for rate-independent plasticity of polycrystals. European Journal of Mechanics A/Solids 28:905–915.

Yoshida, K., Kuroda, M. (2012). Comparison of bifurcation and imperfection analyses of localized necking in rate-independent polycrystalline sheets. International Journal of Solids and Structures 49:2073–2084.

Appendix A

The set of FCC slip systems is given in the table below:

α	1	2	3	4	5	6
$\sqrt{3}\vec{\boldsymbol{m}}_0^{\,\alpha}$	[0 –1 1]	[1 0 1]	[1 1 0]	[0 –1 1]	[–1 0 1]	[1 –1 0]
$\sqrt{2}\vec{\boldsymbol{n}}_0^{\,\alpha}$	(–1 1 1)	(–1 1 1)	(–1 1 1)	(1 1 1)	(1 1 1)	(1 1 1)
α	7	8	9	10	11	12
$\sqrt{3}\vec{\boldsymbol{m}}_0^{\,\alpha}$	[0 1 1]	[1 0 1]	[1 –1 1]	[0 1 1]	[–1 0 1]	[1 1 0]
$\sqrt{2}\vec{\boldsymbol{n}}_0^{\,\alpha}$	(1 1 –1)	(1 1 –1)	(1 1 –1)	(1 –1 1)	(1 –1 1)	(1 –1 1)

Table A.1: List of FCC slip systems related to the intermediate configuration.

The hardening matrix used in this study is of power-law type, which is given by the following relations:

$$H^{\alpha\beta} = h_0\left(1+\frac{h_0\Gamma}{\tau_0 n_1}\right)^{n_1-1} \quad ; \quad \Gamma = \int_0^t \sum_{\alpha=1}^{N_g} \dot{\gamma}^{\alpha} dt \tag{A.1}$$

where τ_0 is the initial critical shear stress, h_0 is the initial hardening rate and n_1 is the power-law hardening exponent.